Correspondence to:
X. Guo,
gxzhuan@mail.gyig.ac.cn

CO_2 Induced a Small Water Solubility in Orthopyroxene and Its Implications for Water Storage in the Upper Mantle

Xinzhuan Guo[1] (ID), Jiayuan Bai[2] (ID), Chao Wang[2], Xiang Wu[2] (ID), and Xingfan Zhou[2]

[1]Key Laboratory for High-Temperature and High-Pressure Study of the Earth's Interior, Institute of Geochemistry, Chinese Academy of Sciences, Guiyang, China, [2]State Key Laboratory of Geological Processes and Mineral Resources, China University of Geosciences, Wuhan, China

Abstract To investigate the effect of CO_2 on water solubility in orthopyroxene coexisting with H_2O-CO_2 as a buffering fluid, high-pressure experiments were conducted at pressures of 1.5 and 3 GPa and a temperature of 1100 °C. The experiments were performed in a Walker-type multianvil assembly using natural orthopyroxene with various CO_2 to CO_2-H_2O molar ratios as a starting material. The water contents were measured by polarized Fourier transform infrared spectrometry. At 1.5 GPa and 1100 °C, the H_2O solubility decreased with increasing CO_2 content in the fluid. The water solubility $c(H_2O)$ could be quantitatively determined based on water fugacity $f(H_2O)$ as $c(H_2O) = 25.21 \times f(H_2O)^{1.24}$. The addition of 57% CO_2 dramatically reduced the water solubility in orthopyroxene from 184 to 90 ppm. In contrast, at 3 GPa and 1100 °C, the water solubility did not change with the CO_2 content in the starting material because CO_2 is unstable in bulk peridotite due to the reaction between CO_2 and olivine at pressures exceeding 2.2 GPa. This study confirms that the additional component in the aqueous fluid can change the water activity and fugacity, thereby directly lowering the water storage capacity in mantle minerals. As a result, previous estimates of the maximum water storage capacity in the shallow mantle may be overestimated by a factor of 3.

1. Introduction

The mantle is potentially a huge water reservoir in deep Earth, and this reservoir has important effects on water distribution and water cycling, including the formation of the Earth's hydrosphere and atmosphere (Bell & Rossman, 1992; Hirschmann, 2006). Water is mainly stored in nominally anhydrous minerals as H-related point defects such as OH groups. The structural hydrogen in nominally anhydrous minerals can significantly affect the melting points of minerals (Gaetani & Grove, 1998), viscosity (Mackwell et al., 1985; Mei & Kohlstedt, 2000a, 2000b; Tielke et al., 2017), and electrical conductivity (Karato, 1990; Yoshino et al., 2006). Therefore, it is important to investigate water solubility in mantle minerals.

Most experimental studies on water solubility in mantle minerals were carried out under pure water-saturated conditions (Bai & Kohlstedt, 1992, 1993; Férot & Bolfan-Casanova, 2012; Gaetani et al., 2014; Kohlstedt et al., 1996; Matveev, 2001; Mierdel et al., 2007; Mierdel & Keppler, 2004; Padron-Navarta & Hermann, 2017). However, the fluid environment of the upper mantle is complex. The shallow fluid in the upper mantle is mainly H_2O-CO_2 (Baptiste et al., 2015), while the deep fluid is CH_4-H_2O (Frost & McCammon, 2008; Wood et al., 1990; Yang, 2015; Yang et al., 2014). Yang et al. (2014) and Yang (2015) experimentally studied water solubility in olivine with H_2O-CO_2 or H_2O-CH_4 as the buffering fluid. Compared with pure water environments, the addition of CO_2 or CH_4 strongly reduced the water solubility of olivine, indicating that the storage capacity of water in the shallow mantle estimated using pure water as the buffering fluid may be largely overestimated.

Next to olivine, pyroxene is the most important constituent of the upper mantle. The maximum water solubility of orthopyroxene is higher than that of olivine under the conditions of the shallow upper mantle (e.g., pressure < 5 GPa; Hauri et al., 2006). The hydrogen incorporation mechanism in orthopyroxene has been widely investigated (Rauch & Keppler, 2002; Stalder, 2004; Stalder et al., 2005; Stalder et al., 2015). If some amount of aluminum (Al) is incorporated into the crystal structure, the water solubility could increase significantly. For example, approximately 1 wt% Al_2O_3 enhanced the water solubility of enstatite from 199 to

Table 1
Summary of Experimental Conditions and Results

Run no.	P (GPa)	Fluid composition (in weight)	Fluid source	Duration (hr)	ppm H_2O[a]
R1026	1.5	(H_2O) 100%	Talc + brucite	28	184 ± 10
PC494	1.5	(H_2O) 82%, (CO_2) 18%	Talc + brucite + oxalic acid	28	149 ± 8
PC489	1.5	(H_2O) 66%, (CO_2) 34%	Talc + brucite + oxalic acid	28	124 ± 12
R1026	1.5	(H_2O) 43%, (CO_2) 57%	Talc + brucite + oxalic acid	28	90 ± 3
R1060	3	(H_2O) 100%	Talc + brucite	28	363 ± 36
R1072	3	(H_2O) 82%, (CO_2) 18%	Talc + brucite + oxalic acid	28	364 ± 50
R1060	3	(H_2O) 66%, (CO_2) 34%	Talc + brucite + oxalic acid	28	364 ± 37
R1072	3	(H_2O) 43%, (CO_2) 57%	Talc + brucite + oxalic acid	28	365 ± 39
En1[b]	1.5	(H_2O) 100%	Mg $(OH)_2$ + SiO_2	94	199 ± 15
En6[b]	3	(H_2O) 100%	Mg $(OH)_2$ + SiO_2	144	372 ± 20

Note. All runs experiments were carried out at 1100 °C, and oxygen fugacity of the sample was controlled by Ni-NiO buffer.
[a]Based on the absorption coefficient of Bell et al. (1995).   [b]Data from Rauch and Keppler (2002); both experiments are conducted at 1100 °C and buffered by Ni-NiO.

1,100 ppm at 1100 °C and 1.5 GPa (Rauch & Keppler, 2002). The partition coefficient of water in Al-rich orthopyroxene to olivine ($D_{H_2O}^{Opx}$) is as high as 11.7 (Grant et al., 2007). Therefore, orthopyroxene might be a more important water host than olivine in the shallow upper mantle. The lower H_2O activity and H_2O fugacity in H_2O-CO_2 fluid could potentially reduce the H_2O solubility of orthopyroxene, as has been confirmed for olivine (Yang et al., 2014). Thus, to properly evaluate water storage in the upper mantle, experiments on the water solubility of orthopyroxene in complex fluids, particularly C-H-O fluid, should be performed.

In this study, we investigated the water solubility in single-crystal orthopyroxene coexisting with peridotite powder and H_2O-CO_2 fluid at 1.5 and 3 GPa and 1100 °C with oxygen fugacity buffered by Ni-NiO. For comparison, experiments on water solubility in orthopyroxene coexisting with H_2O alone were also conducted. The influence of CO_2 on water storage in the upper mantle is discussed on the basis of these experiments. The results of this study improve our understanding of water storage in the upper mantle in terms of water fugacity and pressure.
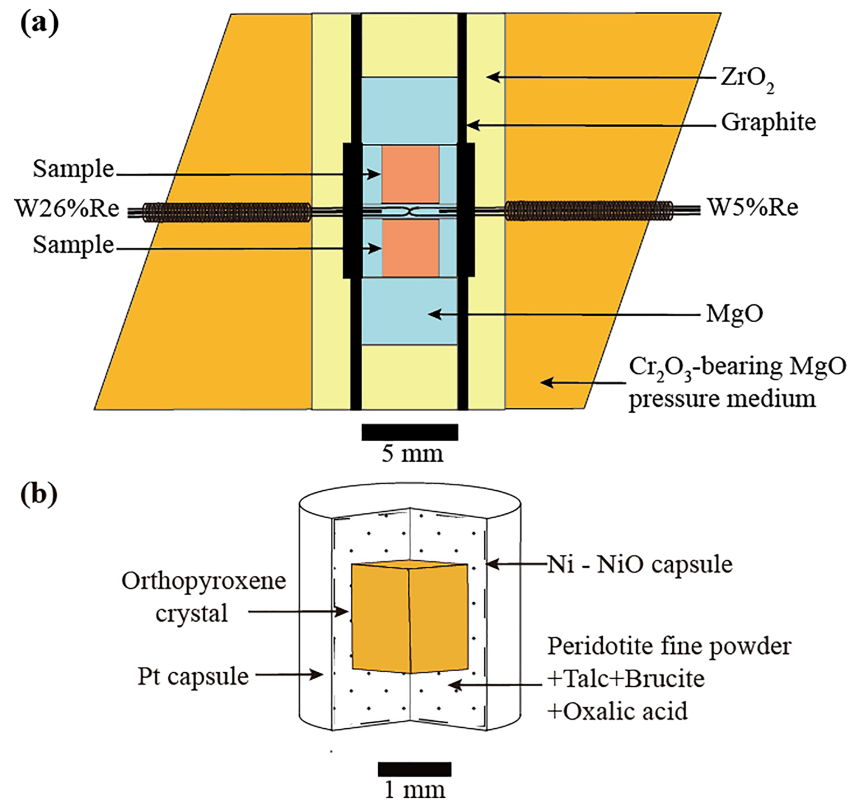
2. Experimental Methods

2.1. Starting Materials

Natural single-crystal orthopyroxene was separated from a spinel-bearing lherzolite xenolith sampled at Damaping (Hannuoba area, Hebei Province, China). Polarized Fourier transform infrared (FTIR) spectroscopy measurements yielded a water content of 39 ppm by weight in the single-crystal orthopyroxene. The orthopyroxene crystal was cut into blocks with dimensions of $1 \times 1 \times 1.5$ mm to prepare the water adopter in the experiments. Another spinel-bearing lherzolite collected from Damaping and consisting of olivine (66 vol%), orthopyroxene (24 vol%), clinopyroxene (8 vol%), and ferran spinel (2 vol%) was milled into powder with a grain size of less than 20 μm. The powders were then mixed with brucite, talc, and oxalic acid ground in an agate mortar. These powders were used in experiments to construct peridotite-saturated conditions. Brucite and talc with a molar radio of 5:1 were used as the water source, and oxalic acid was used as both the H_2O and CO_2 sources. The chemical composition of single-crystal orthopyroxene is similar to that of the matrix orthopyroxene. It should be noted that oxalic acid decomposes to CO_2, H_2O, and CO at ambient pressure and high temperature. However, under our experimental conditions of 1.5 and 3 GPa and 1100 °C, the oxygen fugacity of Ni-NiO lies mostly within ± 1.18 log units relative to the fayalite-magnetite-quartz buffer according to the formula of Dai et al. (2016). Under these conditions, CO will be oxidized to CO_2 (Zhang & Duan, 2010). The bulk H_2O content in all experimental runs was 5 wt%, and the CO_2 content in the fluid, X (CO_2), varied from 0% to 57%. Detailed information about the starting materials is provided in Table 1.

2.2. High-Pressure Experiments

All experiments were conducted using a Walker-type Rockland 1,000-ton multianvil apparatus at the State Key Laboratory of Geological Processes and Mineral Resources, China University of Geosciences (Wuhan).

Figure 1. (a) Schematic cross section of the cell assembly for the Walker-type apparatus and (b) detailed schematic of the experimental capsule.

A Cr_2O_3-doped MgO octahedron with an edge length of 25 mm was adopted as a pressure medium. Eight tungsten carbide anvils with a truncation of 15 mm were used as the second-stage anvils. Pressure generation in this 25/15 assembly was determined previously based on the phase transition of Bi and the melting of NaCl (Li et al., 2018). The detailed cell design is shown in Figure 1.

The stepped heater can effectively reduce the temperature gradient within the cell. Orthopyroxene crystal was embedded in the peridotite matrix, in which the water and CO_2 sources were homogeneously mixed. The Ni-NiO capsule was placed inside the Pt capsule. This double-capsule assemblage can efficiently buffer the oxygen fugacity and prevent water loss during high-temperature experiments. To ensure the equilibrium of hydrogen between the orthopyroxene crystals and the matrix, the experimental duration was set at 28 hr based on the calibration of the H_2O diffusion distance under a hydrogen diffusion coefficient of 1.3×10^{-11} m^2/s at 1100 °C (Carpenter Woods, 2001; Denis et al., 2018). The experimental conditions are listed in Table 1.

2.3. Analytical Techniques

After annealing experiments, the recovered capsules were first mounted in epoxy resin and then polished on one side using sandpapers (#600, #2000, and #5000) under dry conditions and Al_2O_3 polishing slurry (1 and 0.05 μm) in sequence until the surface of orthopyroxene crystal could be clearly observed.

The recovered single-crystal orthopyroxene was cut into three individual parts along random but mutually perpendicular directions. Every sample was then double-polished to a thickness of 150–200 μm. Polarized FTIR spectroscopy spectra were acquired using a Nicolet 6700 spectrometer equipped with a Nicolet continuum microscope, a KBr beam splitter, and a liquid nitrogen-cooled MCT-A detector at the State Key Laboratory of Geological Processes and Mineral Resources, China University of Geosciences (Wuhan). The polarized spectra were obtained with the electric field vector (E) parallel to two mutually perpendicular directions. The aperture size was 50×50 μm or 100×100 μm. For all measurements, 256 scans were

collected in transmission mode in the wavenumber range of 650–4,000 cm^{-1} at a resolution of 4 cm^{-1}. The spectral backgrounds were corrected by the spline fitting of the baseline defined by points outside the OH-stretching region.

The water content of orthopyroxene, an anisotropic mineral, can be determined from the polarized spectra of three random (x, y, and z) but orthogonal sections of the crystal (Libowitzky & Rossman, 1996; Shuai & Yang, 2017). The total thickness-normalized integral absorbance (Abs_{tot}) can be expressed as

$$Abs_{tot} = Abs_x + Abs_y + Abs_z \qquad (1)$$

with

$$Abs_x = \frac{Abs_{max,x} + Abs_{min,x}}{2}, \qquad (2)$$

$$Abs_y = \frac{Abs_{max,y} + Abs_{min,y}}{2}, \qquad (3)$$

and

$$Abs_z = \frac{Abs_{max,z} + Abs_{min,z}}{2}. \qquad (4)$$

The water content (C_w, in ppm) can be determined by the Beer-Lambert law, $C_w = Abs_{tot}/I'$, where I' is the mineral-specific integral molar absorption coefficient (ppm^{-1}·cm^{-2}). In this study, I' was 15.6 ± 0.94 ppm^{-1}·cm^{-2} according to the calibration of Bell et al. (1995). This method has been efficiently used to measure the water contents of monoclinic minerals including feldspars (Johnson & Rossman, 2003).
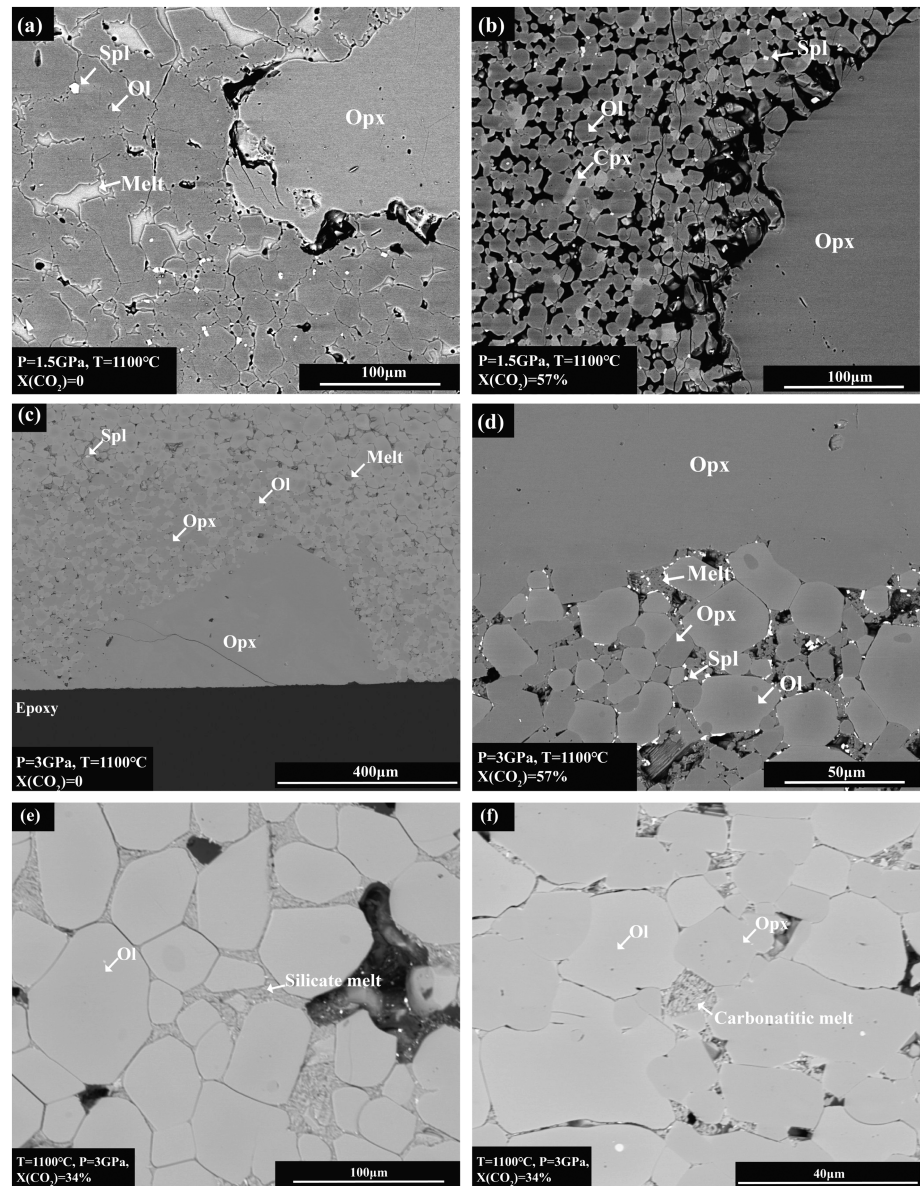
To verify the homogeneity of water in orthopyroxene, FTIR mapping analysis and profile analysis were performed for all sections. The mapping area covered the entire crystal and a part of the peridotite matrix; the step length was 50 or 100 μm, and 64 scans were accumulated for each spot. For line analysis, spectra were collected in the range of 650–4,000 cm^{-1} with an aperture of 100×100 μm from the rim to the core. The step length was 100 μm, and 256 scans were accumulated for each spot.

The contents of major elements in the recovered samples were analyzed using a JEOL-8100 electron microprobe with an accelerating voltage of 15 kV, a beam current of 20 nA, and a beam size of 1–5 μm for mineral analysis; for melt analysis, the beam current and beam size were 10 nA and 7–10 μm, respectively. The textures of the samples were observed by scanning electron microscopy using a Quanta2000 scanning electron microscope.

3. Results

3.1. Textures of the Recovered Samples

The saturation of H_2O was recognized by bubble escaping from the capsule when we pierced the capsule. Under water-saturated conditions, no reaction rim between orthopyroxene crystals and the matrix was observed in any of the annealed samples (Figure 2a), and the chemical compositions before and after annealing were identical (Table 2). In all experiments, partial melting occurred, and clinopyroxene almost disappeared. The relic components in the matrix were olivine, orthopyroxene, spinel, and melts (Figure 2c). The volume fractions of melt in all samples were less than 3%. The melt fraction was independent of X (CO_2) in the sample. According to the melting experiments carried out on a model of the upper mantle (Green, 1973), the solidus of pyrolite under water-saturated conditions is around 950–1000 °C at 1.5 GPa and 1000–1050 °C at 3 GPa, and the disappearance temperature of clinopyroxene is nearly 1100 °C at 1.5 GPa and 1050 °C at 3 GPa. At 2–3 GPa and temperatures below 1000 °C, the melting temperature of peridotite coexisting with both CO_2 and H_2O was found to be lower than that of peridotite coexisting with H_2O alone (Wallace & Green, 1988). The experimental temperature of 1100 °C in this study is greater than the hydrous solidus at both 1.5 and 3 GPa. Therefore, the assemblages of olivine + orthopyroxene + melt are consistent with previous studies.

Figure 2. Scanning electron microscopy images of different products: (a) and (b) annealed at 1.5 GPa and 1100 °C with X (CO_2) = 0% and 57%, respectively. (c) and (d) annealed at 3 GPa and 1100 °C with $X(CO_2)$ = 0% and 57%, respectively. (e) and (f) dendritic melts at 3 GPa. Opx = orthopyroxene; Ol = olivine; Cpx = clinopyroxene; Spl = spinel.

The melt morphology differed between 1.5 and 3 GPa. At 1.5 GPa, the melt was a homogeneous glass (Figure 2a). In contrast, the melt at 3 GPa showed a dendritic texture with two different intergrown components (Figures 2e and 2f). The compositions of these two melts were also very different (Table 3). The melt at 1.5 GPa was a basaltic melt containing 48.2–53.4 wt% SiO_2, while that at 3 GPa had a much lower SiO_2 content (3–28 wt%). CO_2 was experimentally confirmed to react with olivine to produce orthopyroxene and $MgCO_3$ at 2.2 GPa and 1100 °C (Newton & Sharp, 1975). At 3 GPa and 1100 °C in our experiments, the $MgCO_3$ crystals eventually disappeared, and a carbonatitic silicate melt was observed in the H_2O-saturated environment (Dasgupta & Hirschmann, 2007). The carbonatitic melt with very low SiO_2 content was separated from the carbonatitic silicates during quenching, forming the dendritic textures shown in Figure 2f. The amount of $H_2O + CO_2$ dissolved in the melt can be estimated from the difference between 100% and the total $H_2O + CO_2$ observed by microprobe analysis. At 1.5 GPa, the $CO_2 + H_2O$ content of the silicate melt in the matrix was between 8.7 and 15.6 wt%. Considering that the water content of melt in peridotite with a

Table 2
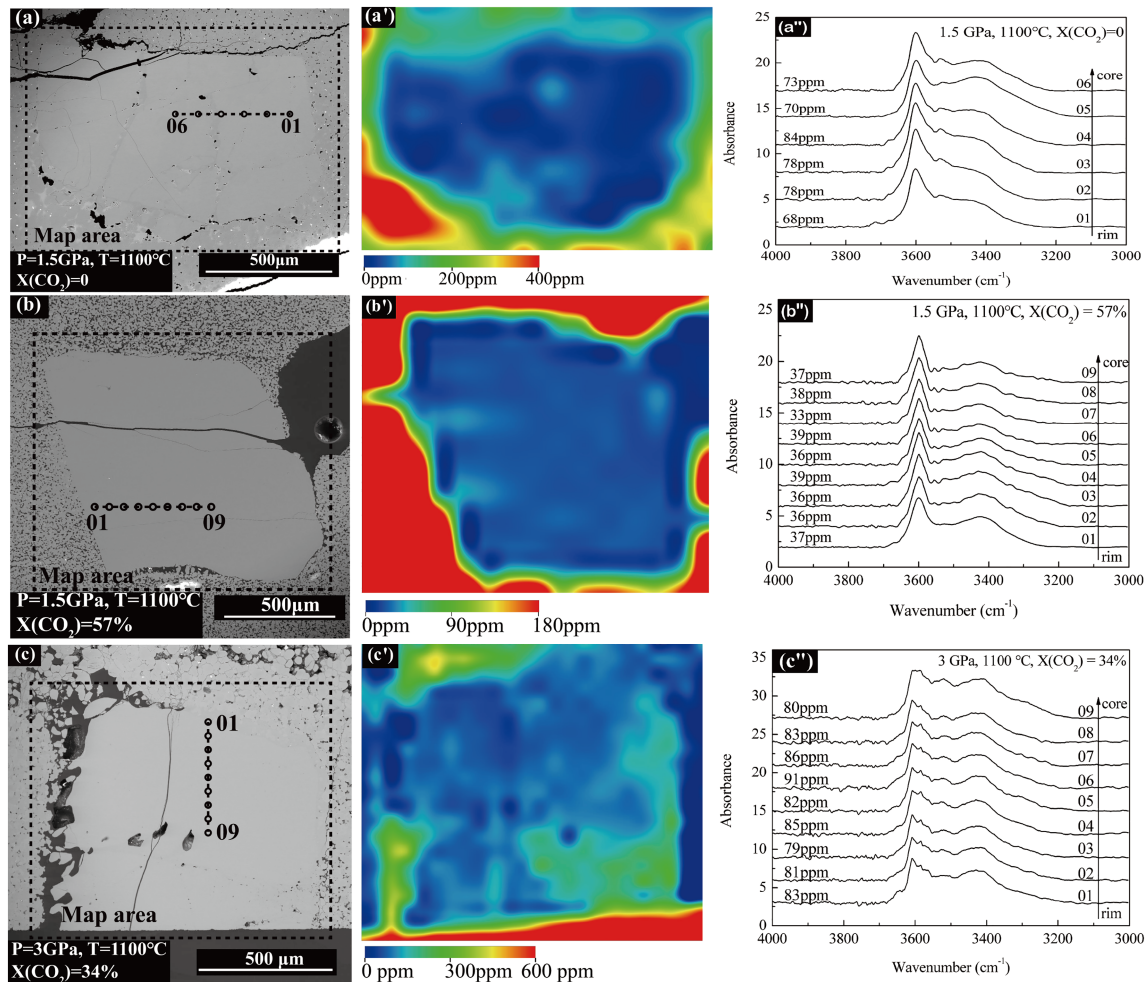*Chemical Compositions of the Starting Materials and the Recovered Samples (wt%)*

	Before experiments				After experiments									
		Peridotite			Orthopyroxene crystals								Peridotite		
Weight (%)	Orthopyroxene crystals	Cpx	Ol	Opx	R1026	PC494	PC489	R1026	R1060	R1072	R1060	R1072	Cpx	Ol	Opx
SiO_2	54.96	52.17	41.96	56.16	55.18	55.70	55.50	54.47	56.19	55.35	55.32	54.70	51.81	40.57	55.83
MgO	33.49	15.41	49.71	33.06	33.88	33.85	33.09	32.83	34.29	32.84	33.09	32.31	14.85	49.06	34.21
K_2O	0.00	0.01	0.01	0.01	0.01	0.00	0.04	0.00	0.01	0.00	0.00	0.00	0.00	0.00	0.00
FeO	5.78	2.35	8.53	6.15	5.60	5.24	5.58	5.37	3.46	5.59	5.89	6.35	2.77	6.56	4.50
Al_2O_3	3.66	5.25	0.02	3.22	3.57	3.59	3.76	4.84	2.01	3.72	4.11	4.54	5.85	0.03	2.98
Na_2O	0.05	1.59	0.01	0.05	0.06	0.08	0.25	0.05	0.01	0.06	0.09	0.10	1.63	0.01	0.03
CaO	0.43	21.03	0.07	0.41	0.50	0.57	0.64	0.54	0.35	0.73	0.58	0.70	21.09	0.06	0.52
Cr_2O_3	0.00	0.89	0.04	0.31	0.00	0.48	0.00	0.49	0.84	0.55	0.42	0.35	0.92	0.08	0.62
TiO_2	0.14	0.37	0.01	0.06	0.08	0.08	0.03	0.20	0.05	0.08	0.12	0.12	0.42	0.01	0.07
MnO	0.14	0.07	0.11	0.13	0.13	0.14	0.13	0.16	0.09	0.14	0.14	0.14	0.07	0.09	0.12
NiO	0.00	0.00	0.00	0.00	0.00	0.26	0.00	0.79	1.86	0.13	0.11	0.12	0.31	3.12	0.62
Total	98.65	99.13	100.46	99.57	99.68	100.00	98.98	99.75	99.16	99.18	99.89	99.42	99.72	99.61	99.49
Total O=	6	6	4	6	6	6	6	6	6	6	6	6	6	4	6
Si	1.92	1.91	1.01	1.94	1.92	1.92	1.93	1.89	1.95	1.92	1.91	1.90	1.89	1.00	1.93
Mg	1.74	0.84	1.79	1.70	1.75	1.72	1.71	1.70	1.77	1.70	1.70	1.67	0.81	1.80	1.76
K	0.00	0.00	0.00	0.00	0.00	0.00	0.00	0.00	0.00	0.00	0.00	0.00	0.00	0.00	0.00
Fe^a	0.17	0.07	0.17	0.18	0.16	0.16	0.16	0.16	0.10	0.16	0.17	0.18	0.08	0.14	0.13
Al	0.15	0.23	0.00	0.13	0.15	0.15	0.15	0.20	0.08	0.15	0.17	0.19	0.25	0.00	0.12
Na	0.00	0.11	0.00	0.00	0.00	0.01	0.02	0.00	0.00	0.00	0.01	0.01	0.12	0.00	0.00
Ca	0.02	0.82	0.00	0.02	0.02	0.02	0.02	0.02	0.01	0.03	0.02	0.03	0.82	0.00	0.02
Cr	0.00	0.03	0.00	0.01	0.00	0.01	0.02	0.01	0.02	0.01	0.01	0.01	0.03	0.00	0.02
Ti	0.00	0.01	0.00	0.00	0.00	0.00	0.00	0.01	0.00	0.00	0.00	0.00	0.01	0.00	0.00
Mn	0.00	0.00	0.00	0.00	0.00	0.00	0.00	0.00	0.00	0.00	0.00	0.00	0.00	0.00	0.00
Ni	0.00	0.00	0.00	0.00	0.00	0.00	0.00	0.02	0.05	0.00	0.00	0.00	0.01	0.06	0.02
Mg#	0.91	0.92	0.91	0.91	0.92	0.92	0.91	0.92	0.95	0.91	0.91	0.90	0.91	0.93	0.93
Total	4.01	4.02	2.98	3.99	4.01	4.00	4.00	4.00	4.00	3.99	4.00	4.00	4.02	3.00	4.00

Note. N denotes the number of analyses for each mineral.
[a] It is assumed that all iron is ferrous iron.

Table 3
Chemical Composition of the Melt (wt%)

	1.5 GPa, 1100 °C				3 GPa, 1100 °C					
					R1072 18% CO_2		R1060 34% CO_2		R1072 57% CO_2	
Weight (%)	R1026 5% H_2O ($N = 5$)	PC 494 18% CO_2 ($N = 3$)	R1026 57% CO_2 ($N = 4$)	R1060 5% H_2O ($N = 5$)	Melt1 ($N = 6$)	Melt2 ($N = 4$)	Melt1 ($N = 5$)	Melt2 ($N = 1$)	Melt1 ($N = 5$)	Melt2 ($N = 5$)
SiO_2	53.38	48.17	51.31	40.18	28.11	19.96	25.74	18.65	13.79	3.29
MgO	9.35	3.36	7.09	8.79	11.21	9.56	11.28	11.59	17.27	18.82
K_2O	0.07	0.19	1.09	0.35	0.28	0.27	0.30	0.14	0.46	0.04
FeO^a	3.97	2.14	2.27	3.74	4.84	3.46	5.85	5.73	5.52	4.86
Al_2O_3	12.22	18.68	18.64	15.70	10.90	7.89	13.02	6.90	7.09	1.49
Na_2O	1.06	0.36	1.59	0.53	0.46	0.48	0.40	0.31	0.26	0.24
CaO	10.13	9.73	6.68	9.68	15.23	20.19	15.43	19.18	18.79	24.11
Cr_2O_3	0.16	0.07	0.02	0.06	0.13	0.07	0.06	0.08	0.05	0.03
TiO_2	0.71	1.21	0.95	0.63	0.90	0.40	0.63	0.32	0.42	0.13
MnO	0.10	0.11	0.05	0.16	0.17	0.17	0.26	0.18	0.29	0.29
NiO	0.13	0.39	0.26	0.97	0.49	0.23	0.23	0.32	0.53	0.53
Total	91.27	84.40	89.96	80.79	72.72	62.67	73.19	63.39	64.47	53.83

Note. N denotes the number of analyses for each melt.
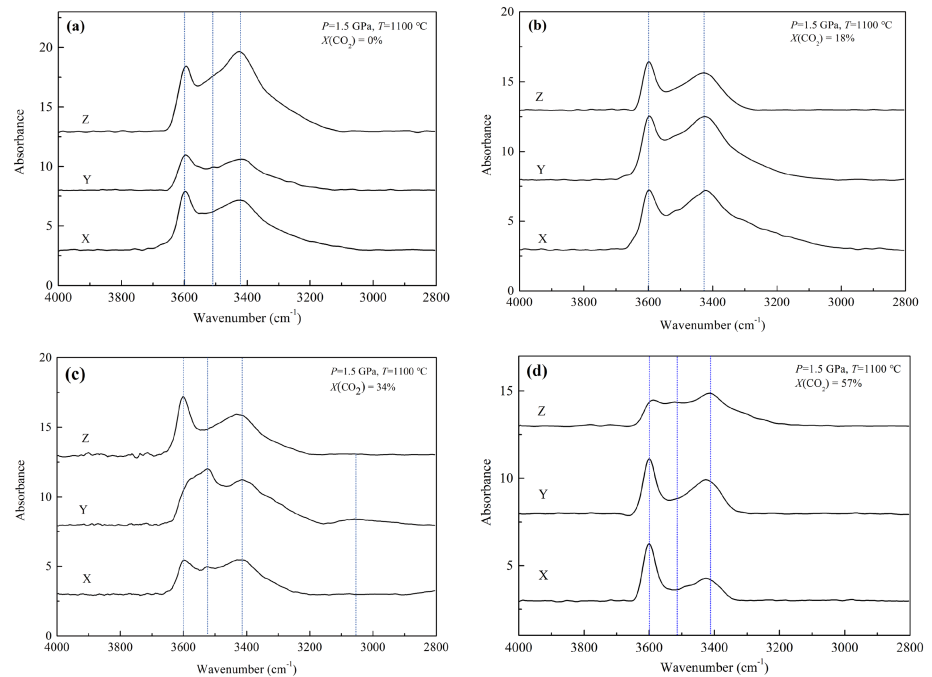[a] It is assumed that all iron is ferrous iron.

Figure 3. Respective FTIR maps and profile spectra of the recovered orthopyroxene crystals. (a–c) Scanning electron microscopy images of the analyzed orthopyroxene samples showing the points of the profile analyses and the areas used for mapping. (a′–c′) FTIR mapping images of the crystals. The water contents are given by the color bar. (a″–c″) Profile analysis results from the rim to the core. The spectra were collected with a spot size of 100 μm and then normalized to a thickness of 1 cm and vertically offset. The numbers above each spectrum give the water contents (left) and the position of the analyzed points (right).

bulk water content of 5 wt% is 8.73 wt%, the CO_2 content of the melt in peridotite with both H_2O and CO_2 at 1.5 GPa was less than 7 wt%. In contrast, the CO_2 + H_2O content of the carbonatitic silicates in peridotite with both H_2O and CO_2 at 3 GPa was much higher (26.81–37.33 wt%).

3.2. FTIR Analysis of Orthopyroxene Crystals

We investigated the zoning in orthopyroxene by FTIR mapping and profile analysis to ensure hydrogen is homogeneously distributed within the orthopyroxene crystal. Figure 3 shows the polarized FTIR mapping results and profile analysis from the rim to the core of the orthopyroxene crystals in one direction (*x*, *y*, or *z*). The water contents given by the color bar in Figure 3 are approximately one third of the total water content. It should be noted that the crystals were easily to be damaged and fractures and cavities would occur during decompressing, especially under 3-GPa condition.

No zoning texture was observed in the OH distribution, and the difference in water content was less than 10%. The green rims (Figures 3a′–3c′) surrounding the crystals can be attributed to the use of the interpolation method when constructing the maps. Therefore, the equilibrium of hydrogen incorporation in orthopyroxene crystals can be established. The crystal quality became worse in the experiments at 3 GPa; more caves were observed within the crystal, resulting in higher water contents in some positions (Figure 3c).
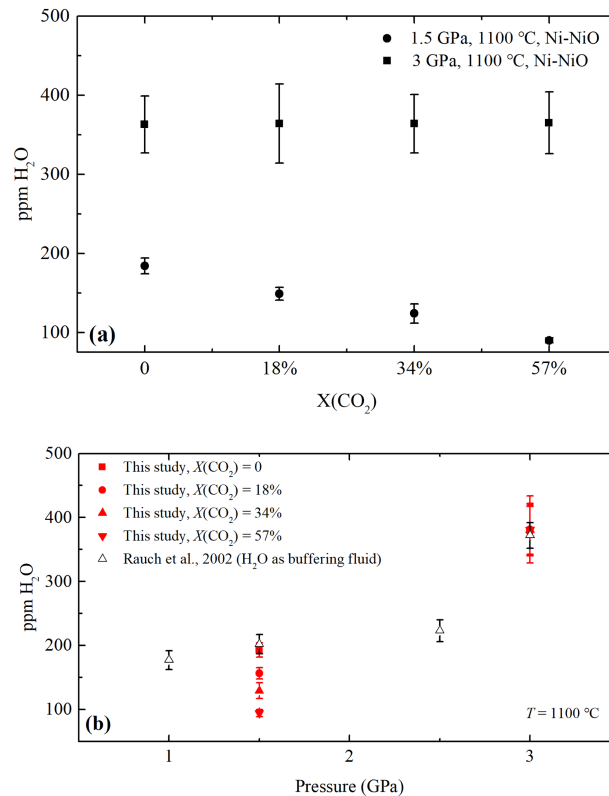
Figure 4. Polarized FTIR spectra of the recovered orthopyroxene crystals normalized to 1-cm thickness. Spectra for three random but mutually perpendicular directions (X, Y, and Z) are offset for clarity. Experimental condition was shown at the top right corner of each panel.

Although no additional experiments with variable durations have been conducted to prove the water equilibration between the crystal and the matrix, we believe the equilibrium has been established for two reasons. (1) The experimental duration of 28 hr is long enough for hydrogen diffusion in both the crystals and the matrix based on the hydrogen diffusivity in these minerals. (2) Profile analysis from the rim to the core and the mapping showed that there are no zoning of water content. In addition, hydrogen equilibrium between olivine and the matrix has been established in experimental studies (Yang, 2015; Yang et al., 2014) within 30 hr at 1.5 GPa, in which experiments the experimental setup was similar to ours. Hydrogen diffusion in orthopyroxene is generally faster than that in olivine. Therefore, the equilibrium should be established in our experiments.

Figure 4 shows representative polarized FTIR spectra of the recovered orthopyroxene on three mutually perpendicular directions (x, y, and z). At 1.5 GPa and 1100 °C, the OH absorption in the orthopyroxene spectra in the mid-IR range (3,700–2,800 cm^{-1}) can be divided into four groups (Figure 4): 3,595–3,600, 3,521, 3,400–3,430, and 3,077 cm^{-1}. The absorption band at 3,595–3,600 cm^{-1} is relatively intense and narrow in all the samples at 1.5 GPa. The absorption band at 3,400–3,430 cm^{-1} is relatively broad. These bands are consistent with natural orthopyroxene in the mantle xenolith (Grant et al., 2007; Yang et al., 2008). The positions of the OH absorption bands in orthopyroxene are almost uniform, regardless of whether CO_2 is present in the fluid (Figure 4). This indicates that the addition of CO_2 to the aqueous fluid does not change the mechanism of hydrogen incorporation in orthopyroxene.

Figure 5 shows the calculated water contents of orthopyroxene crystals as functions of $X(CO_2)$ and pressure. At 1.5 GPa, the H_2O solubility decreased with increasing $X(CO_2)$; the water content decreased from 184 ppm at $X(CO_2) = 0$ to 149 ppm at $X(CO_2) = 18\%$, 124 ppm at $X(CO_2) = 34\%$, and 90 ppm at $X(CO_2) = 57\%$ (Figure 5a). In contrast, at 3 GPa, H_2O solubility in orthopyroxene did not change with the CO_2 content in the fluid. In coexistence with H_2O, the H_2O solubility increased from ~184 ppm at 1.5 GPa to 363 ppm at 3 GPa and 1100 °C; in coexistence with H_2O-CO_2, the H_2O solubility at 3 GPa was at least twice that at 1.5 GPa (Figure 5b). The dependence of $X(CO_2)$ on the H_2O solubility in orthopyroxene is not consistent with that in olivine. Yang et al. (2014) and Yang (2015) reported independent of H_2O solubility in olivine coexisting CH_4-H_2O and CO_2-H_2O fluids at 1.5 and 3 GPa, respectively. In these two studies, the water

Figure 5. Water content of recovered orthopyroxene (a) as a function of $X(CO_2)$ at 1.5 and 3 GPa and 1100 °C and (b) as a function of pressure at 1100 °C.

solubility of olivine first rapidly decreased when additional CO_2 or CH_4 was present, but it was almost independent of $X(CO_2)$ or $X(CH_4)$ when more CO_2 or CH_4 was present. However, the H_2O solubility in orthopyroxene in coexistence with pure H_2O in this study is consistent with those reported by Rauch and Keppler (2002) using the Al-free enstatite as the starting material at both 1.5 and 3 GPa (Figure 5b).
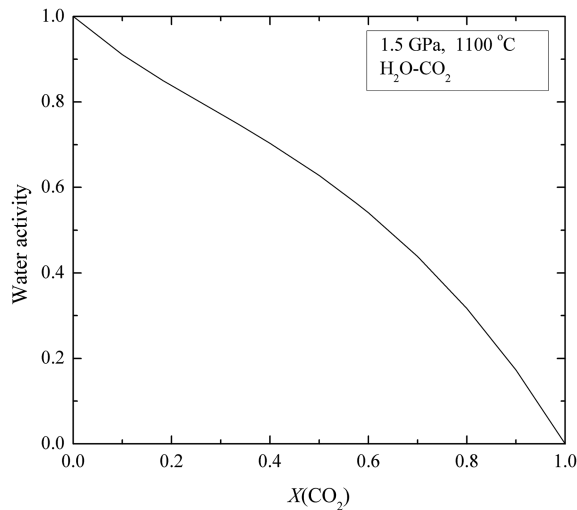
4. Discussion

4.1. OH Groups in Orthopyroxene

The FTIR spectra of orthopyroxene hydrated in equilibrium with either H_2O or H_2O-CO_2 show prominent intrinsic bands of pure enstatite and characteristic Al bands. Pure enstatite exhibits two main OH bands at 3,070 and 3,361 cm^{-1} (Stalder & Skogby, 2002) due to the hydrogen atoms incorporated at the SiO_4- tetrahedron faces pointing toward the cavity between the two M2 positions along the crystallographic b axis. The stretching frequencies of O-H can be calculated from the hydrogen bond length ($d_{O...O}$) (Libowitzky, 1999).

In our samples, Al, Fe, and Cr trivalent cation impurities resulted in complex OH absorption in orthopyroxene. More OH absorption bands are observed at wavenumbers exceeding 3,400 cm^{-1}. The OH absorption band at 3,361 cm^{-1} was either weakened or overwhelmed by the intense absorption at 3,400 cm^{-1}, which was reported in previous studies (Grant et al., 2007; Mierdel et al., 2007). The OH absorption band at 3,070 cm^{-1} is only observed in some of the spectra (sample PC489).

For the OH absorptions at 3,361 and 3,070 cm^{-1}, two possible charge-balancing substitutions are $Si^{4+} = 4H^+$ and $Mg^{2+} = 2H^+$. The absorption bands above 3,400 cm^{-1} are related to Al incorporation in orthopyroxene via three potential mechanisms: $2Al^{3+} \Leftrightarrow Mg^{2+}+Si^{4+}$, $Al^{3+}+H^+ \Leftrightarrow Si^{4+}$, and $Al^{3+}+H^+ \Leftrightarrow 2Mg^{2+}$. When the incorporation mechanism is $Al^{3+}+H^+ \Leftrightarrow Si^{4+}$, hydrogen is mainly incorporated between the oxygen atoms of the SiO_4 tetrahedra, resulting in the additional OH bands above 3,400 cm^{-1} (Stalder, 2004; Stalder & Skogby, 2002). The broad bands in the FTIR spectra of recovered orthopyroxene are attributed to the

Figure 6. Activity-concentration relationship of the CO_2-H_2O system at 1.5 GPa and 1100 °C calculated from the equation of state of binary H_2O-CO_2 (Duan & Zhang, 2006).

crystal distortion resulting from Al substitution (Sakurai et al., 2014). The amount of Cr impurity in our samples was very low; Al/(Al + Cr) was far less than 0.6, indicating that Cr had a negligible influence on the water incorporation mechanism in orthopyroxene (Stalder et al., 2005).

4.2. Effect of H_2O Fugacity on H_2O Solubility in Orthopyroxene

The reduced H_2O solubility in orthopyroxene buffered by bulk peridotite coexisting with H_2O-CO_2 fluid may be related to the reduced water activity and water fugacity due to the addition CO_2 in the fluid at 1.5 GPa and 1100 °C. Oxidized carbon dissolved in pure water can take three forms: carbonate ion (CO_3^{2-}), bicarbonate ion (HCO_3^-), and dissolved CO_2 ($CO_{2,aq}$). Carbonic acid, H_2CO_3, is negligible since it rapidly decomposes in H_2O to produce $CO_{2,aq}$ under high-pressure, high-temperature conditions. High-pressure experiments have shown that the stability of HCO_3^- decreases significantly under high pressure (Martinez et al., 2004). The main oxidized form of carbon is $CO_{2,aq}$ in the H_2O-CO_2 system, and $CO_{2,aq}$ and H_2O are fully miscible under the conditions of the crust or upper mantle (Frantz, 1998; Manning et al., 2013). Given the bulk composition of peridotite, CO_2-H_2O can be stable at pressures up to 2.2 GPa at 1100 °C; in contrast, CO_2 was consumed via reaction with olivine to produce the carbonatitic silicate melt and orthopyroxene at pressures higher than 2.2 GPa and 1100 °C under the water-saturated conditions in our experiments (Dasgupta & Hirschmann, 2007; Newton & Sharp, 1975; White & Wyllie, 1992). Therefore, at 1.5 GPa and 1100 °C, the water activity decreased with increasing CO_2 content. In contrast, the water activity did not change at 3 GPa and 1100 °C, if neglecting the increasing silicate solute in the fluid with increasing pressure.

We calculated the water activity as a function of $X(CO_2)$ at 1.5 GPa and 1100 °C (Figure 6) by applying the equation of state of a binary H_2O-CO_2 system from Duan and Zhang (2006). The water fugacity can be calculated as

$$f(H_2O) = P\Phi_{H_2O}x_{H_2O}, \qquad (5)$$

where P is the pressure (GPa), Φ_{H_2O} is the fugacity coefficient, and x_{H_2O} is the mole fraction of H_2O in the CO_2-H_2O binary system. The calculated water activity and water fugacity values are listed in Table 4.

Figure 7 shows the water content based on the calibration of Bell et al. (1995) against $f(H_2O)$. At a fixed temperature of 1100 °C, water solubility and water fugacity satisfy the following equation:
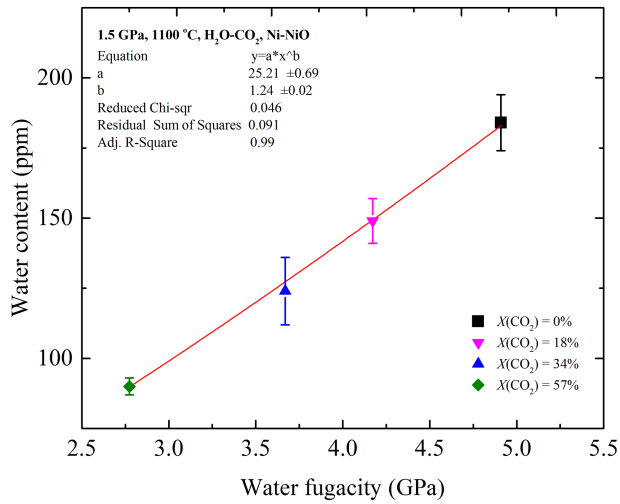
$$c(H_2O) = A \times f(H_2O)^n, \qquad (6)$$

where A is a temperature-dependent constant and n is an exponent depending on the solubility mechanism. The fitted values of A and n are 25.21 ± 0.69 and 1.24 ± 0.02, respectively. Our experiments indicated a strong dependence of water solubility in orthopyroxene on water fugacity at 1.5 GPa. However, no such dependence was observed for olivine buffered by peridotite and H_2O-CO_2 (Yang et al., 2014). In their study, the H_2O solubility in olivine was significantly reduced if CO_2 was added to the fluid; however, H_2O solubility was independent of $X(CO_2)$.

The value of n is related to the incorporation mechanism of water in the minerals (Lu & Keppler, 1997; Rauch & Keppler, 2002). In principle, if H_2O is incorporated through $Mg^{2+} \Leftrightarrow 2H^+$, forming OH pairs, $n = 1$. If H_2O is incorporated through $Si^{4+} \Leftrightarrow 4H^+$, $n = 2$. If the Al^{3+}-related mechanisms ($2Al^{3+} \Leftrightarrow Mg^{2+} + Si^{4+}$, $Al^{3+} + H^+ \Leftrightarrow Si^{4+}$) in orthopyroxene

Table 4
Calculated Results of Water Fugacity at Different $X(CO_2)$

	1.5 GPa, 1100 °C		
$X(CO_2)$	Partial fugacity coefficient φ_i	Water activity a_i	Water fugacity f_i
0.00	3.27	1.00	4.91
0.10	3.31	0.91	4.47
0.18	3.40	0.85	4.17
0.20	3.43	0.84	4.12
0.30	3.61	0.77	3.79
0.34	3.69	0.75	3.67
0.40	3.84	0.70	3.45
0.50	4.11	0.63	3.08
0.57	4.34	0.57	2.77
0.60	4.42	0.54	2.65
0.70	4.78	0.44	2.15
0.80	5.19	0.32	1.56
0.90	5.65	0.17	0.85
1.00	6.19	0.00	0.00

Note. Mole fraction of carbon dioxide. f_i, a_i, and φ_i are the water fugacity, water activity, and water fugacity coefficient of component i at (T, P). The relationship between water fugacity and water activity satisfies $f_i = \varphi_0 P a_i$ (Duan & Zhang, 2006), where φ_0 is the water fugacity coefficient of pure water at (T, P).

Figure 7. Water solubility in orthopyroxene as a function of water fugacity. The red line is the fitting curve with formula $y = ax^b$ ($R^2 = 0.99$).

are dominant, the equilibrium between these two substitution mechanisms can be described by

$$MgAlAlSiO_6 + H_2O + 2Mg_2SiO_4 \Leftrightarrow MgSiO_3 + 2Mg_2AlHSiO_6,$$

with the equilibrium constant

$$K = \frac{a(MgSiO_3)a(Mg_2AlHSiO_6)^2}{a(MgAlAlSiO_6)f(H_2O)a(Mg_2SiO_4)^2},$$

where a is the activity. For this mechanism, $n = 0.5$. The n value in this study was similar to but higher than that obtained for the pure enstatite-H_2O system ($n = 1$; Rauch & Keppler, 2002), indicating a combination of Al^{3+}-related mechanisms ($Al^{3+} + H^+ \Leftrightarrow Si^{4+}$, $Si^{4+} \Leftrightarrow 4H^+$) and Mg^{2+}-related mechanism ($Mg^{2+} \Leftrightarrow 2H^+$). The incorporation mechanism of $Si^{4+} \Leftrightarrow 4H^+$ must be included.

In contrast, at 3 GPa and 1100 °C, CO_2 becomes unstable in bulk peridotite due to its reaction with olivine. As a result, the water activity is approximately 1, and the water fugacity is independent of the $X(CO_2)$ of the starting material. The larger and nearly constant water solubility in orthopyroxene is only due to the higher pressure compared to 1.5 GPa.

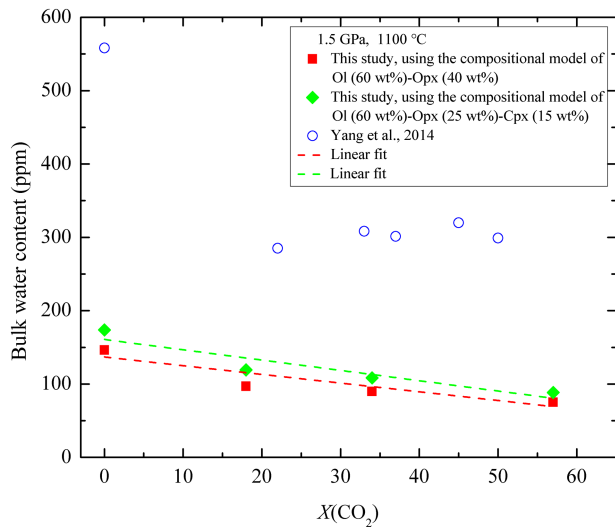### 4.3. Effect of Pressure on H_2O Solubility in Orthopyroxene

The enhanced water solubility in $MgSiO_3$ enstatite with pressure under water-saturated conditions was confirmed at 0.2–10 GPa and 1100 °C by Rauch and Keppler (2002). In our experiments, the H_2O solubility in orthopyroxene with bulk peridotite composition under pure water-saturated conditions increased from ~184 ppm at 1.5 GPa to ~363 ppm at 3 GPa, nearly consistent with the previous study (Table 1 and Figure 5b), in which the starting material was pure enstatite (free of Al^{3+}, Fe^{3+}, and Cr^{3+}). The pressure dependence of water solubility in orthopyroxene is controlled by the combined effect of water fugacity [$f(H_2O)$] and the change in pyroxene volume due to hydrogen incorporation (ΔV), which can be expressed by the solubility law (Lu & Keppler, 1997):

$$c(H_2O) = A'f(H_2O)^n \exp(-P\Delta V/RT), \qquad (7)$$

where A' is a constant depending on T, n is an exponent depending on the solubility mechanism ($n = 1.24$ in this study), and R is the gas constant. It is impossible to evaluate A' and ΔV for orthopyroxene coexisting with peridotite and H_2O-CO_2 fluids because the water solubility is independent of $X(CO_2)$ at pressures higher than 2.2 GPa at the temperature of 1100 °C. Alternatively, the data obtained in aqueous fluid alone were fitting. The fitting results using $n = 1.24 \pm 0.02$ and the water fugacity calculated by Duan and Zhang (2006) yielded $A' = 0.00263$ ppm/bar and $\Delta V = 17.04$ cm^3/mol.

4.4. Maximum Water Storage in the Bulk Shallow Mantle

As mentioned above, lithospheric fluids are very complex in composition. The additional CO_2 phase in aqueous fluids is common in the crust and shallow mantle. The lower water solubility in orthopyroxene in peridotite coexisting with CO_2-H_2O fluids is of significance in understanding water storage in the crust and shallow upper mantle. The water contents in orthopyroxene crystals in this study were much lower than those reported by Hauri et al. (2006) and Mierdel et al. (2007). Considering the effect of CO_2 in the fluid on the water solubility in pyroxene, the maximum water solubility in orthopyroxene reported in previous studies is overestimated by up to two times within the stability field of CO_2 coexisting with bulk peridotite (e.g., pressures below 2.8 GPa at 1200 °C; Newton & Sharp, 1975). Water partition between minerals in the upper mantle has been widely investigated under different conditions (Aubaud et al., 2004; Hauri et al., 2006; Grant et al., 2007; Novella et al., 2014; Sakurai et al., 2014; Demouchy et al., 2017). Among these studies, the experimental condition of Aubaud et al. (2004) is close to ours except that they measured the water content by secondary ion mass spectroscopy rather than FTIR. Given that the partition coefficient

Figure 8. Calculated bulk water content of the shallow upper mantle as a function of $X(CO_2)$ at 1.5 GPa and 1100 °C. The red solid squares represent water content calculated by this study using the compositional model of olivine (60 wt%)-orthopyroxene (40 wt%). The green diamonds represent water content calculated by this study using the compositional model of olivine (60 wt%)-orthopyroxene (25 wt%)-clinopyroxene (15 wt%). The blue open circles represent water content calculated by using water solubility of olivine and partitioning coefficient $D^{Ol/Opx} = 10$ (Yang et al., 2014). Opx = orthopyroxene; Ol = olivine; Cpx = clinopyroxene.

between orthopyroxene and olivine is 10 (Aubaud et al., 2004), the maximum water solubility in olivine coexisting with peridotite and H_2O-CO_2 [$X(CO_2) = 57\%$] fluids should be around 9 ppm at 1.5 GPa. This estimate is five times lower than the experimental result of Yang et al. (2014) under similar experimental conditions, indicating that the partition coefficient of water between orthopyroxene and olivine should be much lower than 10 in peridotite coexisting with H_2O-CO_2 fluids. Considering the experimental results obtained for the peridotite-H_2O-CO_2 system [$X(CO_2) < 57\%$], the maximum partition coefficient is around 4, close to the result of Demouchy et al. (2017). Using the compositional model of olivine (60 wt%)-orthopyroxene (40 wt%), the orthopyroxene data in this study and olivine data from Yang et al. (2014), the water storage capacity of the bulk shallow mantle at 1.5 GPa and 1100 °C decreases from 146 to 75 ppm with increasing $X(CO_2)$ in the fluid from 0% to 57% (Figure 8). If lherzolite model of olivine (60 wt%)-orthopyroxene (25 wt%)-clinopyroxene (15 wt%) together with a water partition coefficient between clinopyroxene and orthopyroxene of 2 was used (Demouchy et al., 2017), the water storage capacity of the bulk shallow upper mantle at 1.5 GPa and 1100 °C decreases from 174 to 89 ppm with increasing $X(CO_2)$ in the fluid from 0% to 57%. These values are just one third of the estimates reported by Yang et al. (2014). Based on the experimental data in this study, it is difficult to evaluate the maximum bulk water content of the deep upper mantle (e.g., pressure > 3 GPa and temperature > 1300 °C for a typical oceanic geotherm; Turcotte & Schubert, 2002) for two reasons: (1) Orthopyroxene crystals are always destroyed by dissolution in melts in the peridotite-H_2O-CO_2 system, making it difficult to measure the water content; and (2) CO_2 is no longer stable under these conditions. However, we can estimate the maximum water storage [$X(CO_2) = 0$] in the bulk mantle at 3 GPa and 1100 °C to be 227–242 ppm. If CH_4-H_2O is considered as a C-H-O fluid in reduced conditions, the water storage capacity of the upper mantle at pressures higher than 3 GPa is expected to decrease with increasing $X(CH_4)$, as reported by Yang (2015).

5. Conclusions

Water solubility in orthopyroxene buffered by peridotite and H_2O-CO_2 fluids was investigated at 1.5 and 3 GPa and 1100 °C using polarized FTIR spectroscopy. The strong effects of water activity and water fugacity on water solubility in orthopyroxene were confirmed in this study. The water fugacity exponent n was determined to be 1.24 at 1.5 GPa and 1100 °C, and the volume change of pyroxene due to hydrogen incorporation (ΔV) was 17.04 cm^3/mol. According to experimental results of this study and Yang et al. (2014), the water partition coefficient between orthopyroxene and olivine is much lower than 10 when these minerals are buffered by the peridotite-H_2O-CO_2 system. Based on our data, the typical compositional model of the upper mantle, and the water solubility in olivine data from Yang et al. (2014), the maximum water storage in bulk shallow mantle is constrained to be less than 0.018 wt% at 1.5 GPa and 1100 °C, which is just one third of the previously estimate reported by Yang et al. (2014).

References

Aubaud, C., Hauri, E. H., & Hirschmann, M. M. (2004). Hydrogen partition coefficients between nominally anhydrous minerals and basaltic melts. *Geophysical Research Letters*, *31*, L20611. https://doi.org/10.1029/2004gl021341

Bai, Q., & Kohlstedt, D. L. (1992). Substantial hydrogen solubility in olivine and implications for water storage in the mantle. *Nature*, *357*, 672–674. https://doi.org/10.1038/357672a0

Bai, Q., & Kohlstedt, D. L. (1993). Effects of chemical environment on the solubility and incorporation mechanism for hydrogen in olivine. *Physics and Chemistry of Minerals*, *19*, 460–471. https://doi.org/10.1007/bf00203186

Baptiste, V., Demouchy, S., Keshav, S., Parat, F., Bolfan-Casanova, N., Condamine, P., & Cordier, P. (2015). Decrease of hydrogen incorporation in forsterite from CO_2-H_2O-rich kimberlitic liquid. *American Mineralogist*, *100*, 1912–1920. https://doi.org/10.2138/am-2015-5200

Bell, D. R., Ihinger, P. D., & Rossman, G. R. (1995). Quantitative analysis of trace OH in garnet and pyroxenes. *American Mineralogist*, *80*, 465–474. https://doi.org/10.2138/am-1995-5-607

Bell, D. R., & Rossman, G. R. (1992). Water in Earth's mantle: The role of nominally anhydrous minerals. *Science*, *255*(5050), 1391–1397. https://doi.org/10.1126/science.255.5050.1391

Carpenter Woods, S. (2001). The kinetics of hydrogen diffusion in single crystal orthopyroxene. Ph.D. thesis. Department of Geosciences, Pennsylvania State University.

Dai, L., Hu, H., Li, H., Wu, L., Hui, K., Jiang, J., & Sun, W. (2016). Influence of temperature, pressure, and oxygen fugacity on the electrical conductivity of dry eclogite, and geophysical implications. *Geochemistry, Geophysics, Geosystems*, *17*, 2394–2407. https://doi.org/10.1002/2016GC006282

Dasgupta, R., & Hirschmann, M. M. (2007). Effect of variable carbonate concentration on the solidus of mantle peridotite. *American Mineralogist*, *92*, 370–379. https://doi.org/10.2138/am.2007.2201

Demouchy, S., Shcheka, S., Denis, C. M. M., & Thoraval, C. (2017). Subsolidus hydrogen partitioning between nominally anhydrous minerals in garnet-bearing peridotite. *American Mineralogist*, *102*(9), 1822–1831. https://doi.org/10.2138/am-2017-6089

Denis, C. M. M., Demouchy, S., & Alard, O. (2018). Heterogeneous hydrogen distribution in orthopyroxene from veined mantle peridotite (San Carlos, Arizona): Impact of melt-rock interactions. *Lithos*, *302*, 298–311. https://doi.org/10.1016/j.lithos.2018.01.007

Duan, Z., & Zhang, Z. (2006). Equation of state of the H_2O, CO_2, and H_2O–CO_2 systems up to 10 GPa and 2573.15 K: Molecular dynamics simulations with ab initio potential surface. *Geochimica et Cosmochimica Acta*, *70*, 2311–2324. https://doi.org/10.1016/j.gca.2006.02.009

Férot, A., & Bolfan-Casanova, N. (2012). Water storage capacity in olivine and pyroxene to 14 GPa: Implications for the water content of the Earth's upper mantle and nature of seismic discontinuities. *Earth and Planetary Science Letters*, *349-350*, 218–230. https://doi.org/10.1016/j.epsl.2012.06.022

Frantz, J. D. (1998). Raman spectra of potassium carbonate and bicarbonate aqueous fluids at elevated temperatures and pressures: Comparison with theoretical simulations. *Chemical Geology*, *152*, 211–225. https://doi.org/10.1016/S0009-2541(98)00058-8

Frost, D. J., & McCammon, C. A. (2008). The redox state of Earth's mantle. *Annual Review of Earth and Planetary Sciences*, *36*, 389–420. https://doi.org/10.1146/annurev.earth.36.031207.124322

Gaetani, G. A., & Grove, T. L. (1998). The influence of water on melting of mantle peridotite. *Contributions to Mineralogy and Petrology*, *131*, 323–346. https://doi.org/10.1007/s004100050396

Gaetani, G. A., O'Leary, J. A., Koga, K. T., Hauri, E. H., Rose-Koga, E. F., & Monteleone, B. D. (2014). Hydration of mantle olivine under variable water and oxygen fugacity conditions. *Contributions to Mineralogy and Petrology*, *167*(2), 1–14. https://doi.org/10.1007/s00410-014-0965-y

Grant, K., Ingrin, J., Lorand, J. P., & Dumas, P. (2007). Water partitioning between mantle minerals from peridotite xenoliths. *Contributions to Mineralogy and Petrology*, *154*, 15–34. https://doi.org/10.1007/s00410-006-0177-1

Green, D. H. (1973). Experimental melting studies on a model upper mantle composition at high pressure under water-saturated and water-undersaturated conditions. *Earth and Planetary Science Letters*, *19*, 37–53. https://doi.org/10.1016/0012-821x(73)90176-3

Hauri, E., Gaetani, G., & Green, T. (2006). Partitioning of water during melting of the Earth's upper mantle at H_2O-undersaturated conditions. *Earth and Planetary Science Letters*, *248*, 715–734. https://doi.org/10.1016/j.epsl.2006.06.014

Hirschmann, M. M. (2006). Water, melting, and the deep earth H_2O cycle. *Annual Review of Earth and Planetary Sciences*, *34*, 629–653. https://doi.org/10.1146/annurev.earth.34.031405.125211

Johnson, E. A., & Rossman, G. R. (2003). The concentration and speciation of hydrogen in feldspars using FTIR and ^{1}H MAS NMR spectroscopy. *American Mineralogist*, *88*, 901–911. https://doi.org/10.2138/am-2003-5-620

Karato, S. (1990). The role of hydrogen in the electrical conductivity of the upper mantle. *Nature*, *347*, 272–273. https://doi.org/10.1038/347272a0

Kohlstedt, D. L., Keppler, H., & Rubie, D. C. (1996). Solubility of water in the α, β and γ phases of $(Mg,Fe)_2SiO_4$. *Contributions to Mineralogy and Petrology*, *123*, 345–357. https://doi.org/10.1007/s004100050161

Li, P., Guo, X., Chen, S., Wang, C., Yang, J., & Zhou, X. (2018). Electrical conductivity of the plagioclase–NaCl–water system and its implication for the high conductivity anomalies in the mid-lower crust of Tibet Plateau. *Contributions to Mineralogy and Petrology*, *173*(2), 1–12. https://doi.org/10.1007/s00410-018-1442-9

Libowitzky, E. (1999). Correlation of O-H stretching frequencies and O-H ... O hydrogen bond lengths in minerals. *Monatshefte für Chemie*, *130*(8), 1047–1059. https://doi.org/10.1007/BF03354882

Libowitzky, E., & Rossman, G. R. (1996). Principles of quantitative absorbance measurements in anisotropic crystals. *Physics and Chemistry of Minerals*, *23*, 319–327. https://doi.org/10.1007/bf00199497

Lu, R., & Keppler, H. (1997). Water solubility in pyrope to 100 kbar. *Contributions to Mineralogy and Petrology*, *129*, 35–42. https://doi.org/10.1007/s004100050321

Mackwell, S. J., Kohlstedt, D. L., & Paterson, M. S. (1985). The role of water in the deformation of olivine single crystals. *Journal of Geophysical Research*, *90*, 1319–1333. https://doi.org/10.1029/JB090iB13

Manning, C. E., Shock, E. L., & Sverjensky, D. A. (2013). The chemistry of carbon in aqueous fluids at crustal and upper-mantle conditions: Experimental and theoretical constraints. *Reviews in Mineralogy and Geochemistry*, *75*, 109–148. https://doi.org/10.2138/rmg.2013.75.5

Martinez, I., Sanchez-Valle, C., Daniel, I., & Reynard, B. (2004). High-pressure and high-temperature Raman spectroscopy of carbonate ions in aqueous solution. *Chemical Geology*, *207*, 45–58. https://doi.org/10.1016/j.chemgeo.2004.02.003

Matveev, S. (2001). Effect of silica activity on OH^- IR spectra of olivine: Implications for low $aSiO_2$ mantle metasomatism. *Journal of Petrology*, *42*, 721–729. https://doi.org/10.1093/petrology/42.4.721

Mei, S., & Kohlstedt, D. L. (2000a). Influence of water on the plastic deformation of olivine aggregates: 1. Diffusion creep regime. *Journal of Geophysical Research*, *105*, 21,457–21,469. https://doi.org/10.1029/2000JB900179

Mei, S., & Kohlstedt, D. L. (2000b). Influence of water on plastic deformation of olivine aggregates: 2. Dislocation creep regime. *Journal of Geophysical Research*, *105*, 21,471–21,481. https://doi.org/10.1029/2000JB900180

Mierdel, K., & Keppler, H. (2004). The temperature dependence of water solubility in enstatite. *Contributions to Mineralogy and Petrology*, *148*, 305–311. https://doi.org/10.1007/s00410-004-0605-z

Mierdel, K., Keppler, H., Smyth, J. R., & Langenhorst, F. (2007). Water solubility in aluminous orthopyroxene and the origin of Earth's asthenosphere. *Science*, *315*(5810), 364–368. https://doi.org/10.1126/science.1135422

Newton, R. C., & Sharp, W. E. (1975). Stability of forsterite + CO_2 and its bearing on the role of CO_2 in the mantle. *Earth and Planetary Science Letters*, *26*, 239–244. https://doi.org/10.1016/0012-821X(75)90091-6

Novella, D., Frost, D. J., Hauri, E. H., Bureau, H., Raepsaet, C., & Roberge, M. (2014). The distribution of H2O between silicate melt and nominally anhydrous peridotite and the onset of hydrous melting in the deep upper mantle. *Earth and Planetary Science Letters*, *400*, 1–13. https://doi.org/10.1016/j.epsl.2014.05.006

Padron-Navarta, J. A., & Hermann, J. (2017). A subsolidus olivine water solubility equation for the Earth's upper mantle. *Journal of Geophysical Research: Solid Earth*, *122*, 9862–9880. https://doi.org/10.1002/2017JB014510

Rauch, M., & Keppler, H. (2002). Water solubility in orthopyroxene. *Contributions to Mineralogy and Petrology*, *143*, 525–536. https://doi.org/10.1007/s00410-002-0365-6

Sakurai, M., Tsujino, N., Sakuma, H., Kawamura, K., & Takahashi, E. (2014). Effects of Al content on water partitioning between orthopyroxene and olivine: Implications for lithosphere-asthenosphere boundary. *Earth and Planetary Science Letters*, *400*, 284–291. https://doi.org/10.1016/j.epsl.2014.05.041

Shuai, K., & Yang, X. (2017). Quantitative analysis of H-species in anisotropic minerals by polarized infrared spectroscopy along three orthogonal directions. *Contributions to Mineralogy and Petrology*, *172*(2-3), 1–17. https://doi.org/10.1007/s00410-017-1336-2

Stalder, R. (2004). Influence of Fe, Cr and Al on hydrogen incorporation in orthopyroxene. *European Journal of Mineralogy*, *16*, 703–711. https://doi.org/10.1127/0935-1221/2004/0016-0703

Stalder, R., Karimova, A., & Konzett, J. (2015). OH-defects in multiple-doped orthoenstatite at 4–8 GPa: Filling the gap between pure and natural systems. *Contributions to Mineralogy and Petrology*, *169*(4), 38–10. https://doi.org/10.1007/s00410-015-1133-8

Stalder, R., Klemme, S., Ludwig, T., & Skogby, H. (2005). Hydrogen incorporation in orthopyroxene: Interaction of different trivalent cations. *Contributions to Mineralogy and Petrology*, *150*(5), 473–485. https://doi.org/10.1007/s00410-005-0037-4

Stalder, R., & Skogby, H. (2002). Hydrogen incorporation in enstatite. *European Journal of Mineralogy*, *14*, 1139–1144. https://doi.org/10.1127/0935-1221/2002/0014-1139

Tielke, J. A., Zimmerman, M. E., & Kohlstedt, D. L. (2017). Hydrolytic weakening in olivine single crystals. *Journal of Geophysical Research: Solid Earth*, *122*, 3465–3479. https://doi.org/10.1002/2017jb014004

Turcotte, D. L., & Schubert, G. (2002). *Geodynamics* (2nd ed., p. 719). Cambridge: Cambridge University Press.

Wallace, M. E., & Green, D. H. (1988). An experimental determination of primary carbonatite magma composition. *Nature*, *335*, 343–346. https://doi.org/10.1038/335343a0

White, B. S., & Wyllie, P. J. (1992). Solidus reactions in synthetic lherzolite-H_2O-CO_2 from 20–30 kbar, with applications to melting and metasomatism. *Journal of Volcanology and Geothermal Research*, *50*, 117–130. https://doi.org/10.1016/0377-0273(92)90040-K

Wood, B. J., Bryndzia, L. T., & Johnson, K. E. (1990). Mantle oxidation state and its relationship to tectonic environment and fluid speciation. *Science*, *248*(4953), 337–345. https://doi.org/10.1126/science.248.4953.337

Yang, X. (2015). OH solubility in olivine in the peridotite-COH system under reducing conditions and implications for water storage and hydrous melting in the reducing upper mantle. *Earth and Planetary Science Letters*, *432*, 199–209. https://doi.org/10.1016/j.epsl.2015.10.014

Yang, X., Liu, D., & Xia, Q. (2014). CO_2-induced small water solubility in olivine and implications for properties of the shallow mantle. *Earth and Planetary Science Letters*, *403*, 37–47. https://doi.org/10.1016/j.epsl.2014.06.025

Yang, X., Xia, Q., Deloule, E., Dallai, L., Fan, Q., & Feng, M. (2008). Water in minerals of the continental lithospheric mantle and overlying lower crust: A comparative study of peridotite and granulite xenoliths from the North China Craton. *Chemical Geology*, *256*, 33–45. https://doi.org/10.1016/j.chemgeo.2008.07.020

Yoshino, T., Matsuzaki, T., Yamashita, S., & Katsura, T. (2006). Hydrous olivine unable to account for conductivity anomaly at the top of the asthenosphere. *Nature*, *443*(7114), 973–976. https://doi.org/10.1038/nature05223

Zhang, C., & Duan, Z. (2010). GFluid: An Excel spreadsheet for investigating C–O–H fluid composition under high temperatures and pressures. *Computers & Geosciences*, *36*, 569–572. https://doi.org/10.1016/j.cageo.2009.05.008